EurJIC
European Journal of Inorganic Chemistry

Research Article
doi.org/10.1002/ejic.202500063

Chemistry Europe
European Chemical Societies Publishing

www.eurjic.org

Pyrazolyl-Pyridine Ruthenium (II) Catalysts for Selective Hydrogen Generation Through Formic Acid Dehydrogenation

Rotondwa Mphephu, M. Cassiem Joseph, and Andrew John Swarts*

A series of pyridine-pyrazolyl Ru(II) p-cymene complexes of the type [RuCl(p-cymene)**L**]X (**C1**–**C7**, X = Cl, BPh_4 or PF_6), featuring different electronic and steric properties, are prepared by the reaction of 3,5-disubstituted pyrazolyl-pyridine ligands (**L1**–**L3**) with $[Ru(p\text{-cymene})Cl_2]_2$ followed by salt metathesis with $NaBPh_4$ or $AgPF_6$. The complexes, upon activation with formate, show activity toward the dehydrogenation of formic acid (FA) to produce equimolar quantities of H_2 and CO_2. In optimization studies, kinetic and thermodynamic investigations provide insight into the role of pre-catalyst and FA in the catalytic process. It is demonstrated that the most active catalyst derived from **C4**, could dehydrogenate FA to CO_2 and H_2 in quantitative yields within 1 h with tons and TOFs of ≈1032 and ≈1238 h^{-1}, respectively. Reactivity patterns are rationalized based on electronic properties and our understanding of ion pairing in related compounds. Reactivity studies between **C4** and HCOOK provide evidence for the key Ru-monohydride species involved in catalysis.

1. Introduction

Global energy consumption, combined with the negative effects of fossil fuels on the climate, has sparked extensive research into sustainable technologies. The use of hydrogen (H_2) as an energy medium is gaining increasing recognition. Hydrogen is a valuable energy source because of its high energy density and clean combustion, as it is accessible through water splitting and only generates benign products upon oxidation in a fuel cell.[1–3] However, the practical use of H_2 is limited due to the associated issues in delivery and storage. Formic acid (FA) has been extensively studied as one of the most promising hydrogen energy carriers today.[4] The catalytic dehydrogenation of FA ideally leads to the formation of CO_2 and H_2 that can be applied in fuel cells. FA contains 4.4 wt% hydrogen and is only moderately harmful to the environment and the human body.[5–7] An additional benefit is that carbon dioxide, which is both abundant and inexpensive, can be utilized as a raw material. In addition, the required energy for mutual conversion with CO_2 in water is −4 kj mol^{-1}, which is substantially lower than that of other H_2 carriers.[8]

Noble metals like iridium (Ir),[9] rhodium (Rh),[10] and ruthenium (Ru)[11] are highly effective in catalyzing formic acid dehydrogenation (FADH). There is great interest in ruthenium complexes due to their outstanding electronic properties, robust coordination chemistry, and ability to withstand a broad range of reaction conditions.[12] In addition, the ligands around these metals influence the activity, selectivity, and stability during catalysis by fine-tuning the electronic and steric properties of the ensuing complexes. By stabilizing key reaction intermediates, the ligand environment not only influences the activation of FA but also optimizes the process of dehydrogenation. For example, Guan et al. showed that by using N,N′-diimine ligand (**Figure 1**a), the ruthenium catalyst, generated via ligand deprotonation, can generate turnover numbers (TONs) of 350,000 and turnover frequency (TOF) of 12,000 h^{-1} at 90 °C in HCOOH/HCOONa aqueous solution.[13,14] Singh and colleagues synthesized water-soluble Ru complexes with N-donor chelating ligands (Figure 1b) for FADH in water and their catalyst demonstrated good catalytic activity, and it can be recycled up to five times, with 2248 TON.[14]

Our group recently used pyridyl-triazole cationic half-sandwich ruthenium complexes bearing alkyl or aryl substituents on the triazole ring, as catalyst precursors for the transfer hydrogenation of acetophenone (Figure 1c). The complexes containing smaller anions (PF_6^- and BF_4^-) were more active catalysts for the transfer hydrogenation of acetophenone than their bph_4^- analogues, regardless of the substituents on the triazole ring. This is due to the formation of contact ion pairs in high dielectric constants, which exert minimal steric hindrance to substrate approach. This allows greater accessibility to the active species and facilitates easier substrate activation.[15] This feature motivated our study to investigate the activity and feasibility of Ru catalysts bearing disubstituted pyrazolyl-pyridine ligands with various anions for the dehydrogenation of FA, which we present herein.

R. Mphephu, M. C. Joseph, A. J. Swarts
Molecular Sciences Institute
School of Chemistry
University of the Witwatersrand
Johannesburg-Braamfontein 2050, South Africa
E-mail: andrew.swarts@wits.ac.za

M. C. Joseph
Department of Chemistry and Polymer Science
Stellenbosch University
Private Bag 1, Matieland, Stellenbosch 7601, South Africa

Supporting information for this article is available on the WWW under https://doi.org/10.1002/ejic.202500063

Research Article
doi.org/10.1002/ejic.202500063

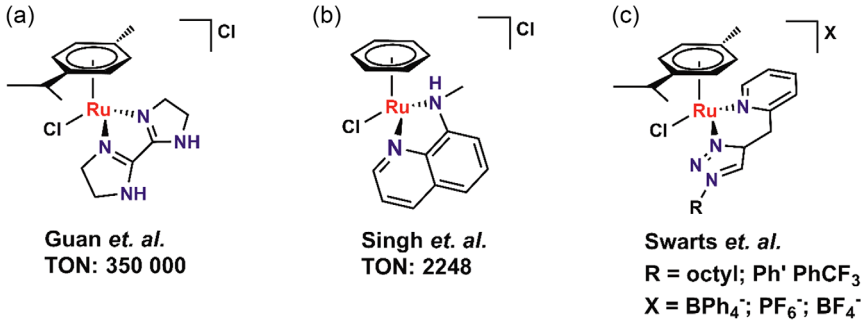

Figure 1. a,b) Ru(II) complexes reported in literature for FADH. c) Triazolylpyridine-ligated Ru(II) complexes which display variable ion-pairing.

2. Results and Discussion

2.1. Synthesis and Characterization of Pyazolyl-Pyridine Ru(II) Complexes

The synthesis of disubstituted (pyrazolyl)pyridine Ru(II) complexes, **C1**–**C7**, commenced with the preparation of pyrazoles, **P2** and **P3**, from the reaction of diketones with hydrazine in ethanol (**Scheme 1**).[16] Subsequent nucleophilic substitution reaction of **P1**-**P3** with (2-bromomethyl)pyridine in the presence of a phase-transfer catalyst afforded the ligands, **L1**–**L3**, in good to moderate yields of 61–88% as brown (**L1**)/yellow oils (**L2**) or white solid (**L3**).[17] **L1**–**L3** were then reacted with dichloro (*p*-cymene)ruthenium(II) dinuclear complex. In methanol at room temperature followed by anion metathesis with $AgPF_6$ or $NaBPh_4$ to afford complexes **C1**–**C7** in good to moderate yields of 72–87% as yellow or orange air- and moisture-stable solids (Scheme 1).[18] Complex composition, atom connectivity, and bulk purity were established with a suite of spectroscopic and analytical techniques.

In the fourier transform infrared (FTIR) spectra of the ligands, the lack of an N-H stretch from the pyrazole (≈3000 cm^{-1}) provided evidence for the successful N-alkylation of the pyrazole. The $\upsilon_{C=N}$ vibrations of both the pyrazole and pyridine rings appear between 1571 and 1593 cm^{-1}. Upon complexation, it is observed that these peaks have blue-shifted to higher frequencies, which confirms coordination and successful complexation.[7] In addition, strong absorption bands are observed in the region 700–756 and 839–840 cm^{-1}, which were assigned to the stretching vibration modes of the B-C and P-F bands of the anions, respectively. The appearance of these absorption bands provided evidence for successful anion exchange of the chloride ligand with the larger anions.

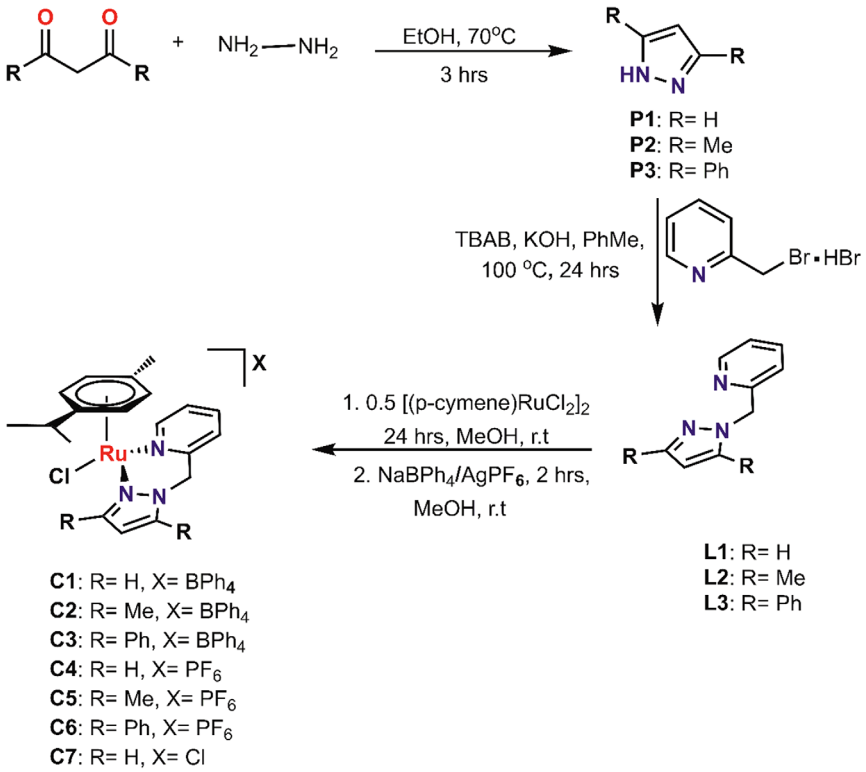

Scheme 1. Synthetic methodology for the synthesis of (pyrazolyl)pyridine-ligated Ru(II) complexes, **C1**–**C7**.

Research Article
doi.org/10.1002/ejic.202500063

Characterization by ^{1}H NMR revealed the presence of the diagnostic N-H singlet of the pyrazole at δ 12.02 and 13.39 ppm for **P2** and **P3**, respectively, indicative of pyrazole formation.[16] The ligands, **L1**–**L3**, showed the disappearance of the diagnostic N-H singlet of the pyrazole, which confirmed the formation of the ligand. The methyl protons of **L2** are observed as inequivalent, indicative of unique, altered electronic environments due to the pyridine-pyrazole linkage. **L1** and **L2** have been previously reported, whereas to the best of our knowledge, **L3** is novel and has not been documented. All ligands exhibit aromatic protons from pyridine, confirming the pyrazole-pyridine linkage.[13] C NMR spectroscopic analysis confirmed the presence of all expected carbon resonances, corroborating the ^{1}H NMR spectral data (Figure S17–S22, Supporting Information). Compared to **L1**, **L2** exhibited new carbon signals between 11.16 and 13.80 ppm, corresponding to the carbon atoms of the methyl groups. Similarly, **L3** displayed additional peaks in the range of 125–133 ppm, which were assigned to the phenyl groups. The mass spectra of all the ligands exhibited the expected base peak, [M$^+$], supporting their proposed molecular compositions (Figure S43–S45, Supporting Information). The bulky purity of **L3** was confirmed by elemental analysis.

The ^{1}H NMR spectrum of the Ru(II) complexes, **C1**–**C7**, showed distinct downfield shifts of key resonances compared to the pyrazole-pyridine ligands, indicative of coordination to the metal centre. The presence of coordinated *p*-cymene contributed additional resonances in the aliphatic and aromatic regions as distinct singlets and multiplets (Figure S24–S41, Supporting Information), with methyl groups of the isopropyl unit (0.90 ppm−2.83 ppm) and aromatic protons of the p-cymene ring (5.0 ppm–6.2 ppm) observed as well-defined singlets and multiplets, reinforcing the coordination of the Ru(II) precursor with the ligand. Based on the bulkiness of the R group on the pyrazole ring, the isopropyl protons of the p-cymene ligand exhibit different splitting patterns. When $R = H$, the isopropyl protons appear as a doublet. However, as the R group increases in size (H < Me < Ph), increased steric interactions lead to a more pronounced diastereotopic effect, resulting in a clear doublet of doublets. This increasing splitting pattern implies restricted rotation and increased asymmetry in the complex as the bulkiness of the substituent increases.

Complexes with $[BPh_4]^-$ (**C1**–**C3**) as the anion showed broader peaks around δ 6.75–7.20 ppm due to the bulkiness of the $[BPh_4]^-$ anion. Additionally, ^{19}F NMR and ^{31}P NMR spectra were measured in order to confirm the presence of $[PF_6]^-$ counterion (Figure S31, S32, S35–S36, S39–S40, Supporting Information). For example, the ^{19}F and ^{31}P NMR spectra of **C4** showed a doublet between −71.08 and −69.19 ppm, and a septet between −157.37 and −131.03 ppm, respectively, ascribed to chemically equivalent fluorine and phosphorus atoms. High-resolution electrospray ionization mass spectrometry (ESI-MS) analysis was conducted in the positive mode, showing the expected base peak, [M$^+$], with characteristic isotopic clusters matching the cationic fragment of the complexes (Figure S46–S52, Supporting Information). Complexes **C1**–**C7** were further characterized by elemental analysis, which confirmed the bulk purity of the complexes.

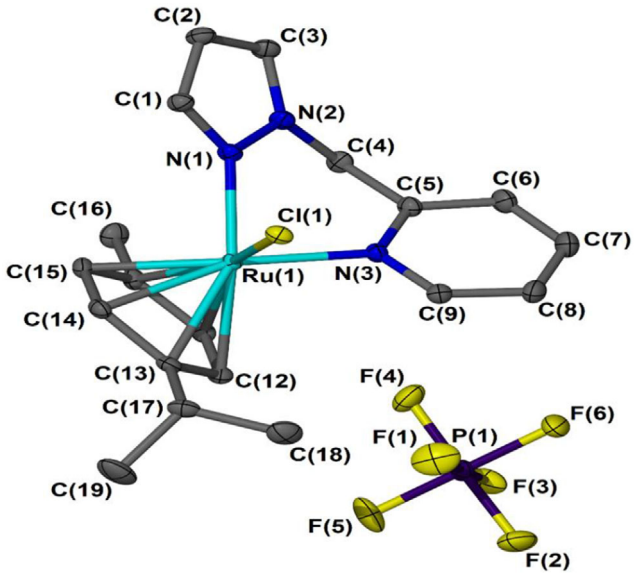

Figure 2. The molecular structures of **C4** with thermal ellipsoids drawn at 30% probability. Hydrogen atoms have been omitted for clarity.

Atom connectivity was unambiguously established for complex **C4** by single crystal X-ray diffraction analysis, from brown single crystals obtained by slow diffusion of diethyl ether into CH_2Cl_2 (see Section S4, Supporting Information). The molecular structure of complex **C4** exhibited a piano-stool octahedral geometry around the metal center as expected for Ru(II) *p*-cymene complexes (**Figure 2**). **C4** was found to crystallize in a triclinic system with space group P-1, with the chloride atom positioned on the opposite side of the isopropyl group of the *p*-cymene, similar to related compounds previously reported.[19,23] Crystallographic data and structure refinement parameters **C4** are shown in Table S1 Supporting Information, while selected bond lengths and angles are given in Table S2, Supporting Information. The Ru–N_{py} and Ru-N_{pz} bond lengths in **C4** range are 2.078 and 2.123 Å, respectively, which is consistent with Ru *p*-cymene/arene compounds reported previously.[20–22] Additionally, the observed N_{py}–Ru–N_{pz} angle is 84.46°, smaller than the ideal geometrical value and reflects the geometric backbone constraint of the chelating ligands, which is known to influence the size of the bite angles of transition metal complexes.[23,24] This value is comparable to Ru *p*-cymene/arene compounds with N,N′ donor ligands.[25,26]

2.2. Electrochemical Analysis

Cyclic voltammetry (CV) was applied to evaluate the redox properties of complexes **C1**–**C7**. Redox potentials were measured using glassy carbon, Pt wire, and Ag/Agcl as the working, counter, and reference electrode, respectively. The electrochemical analysis revealed that all compounds exhibited a reversible redox couple ascribed to Ru^{ii}/Ru^{iii} with $E_{1/2}$ values ranging from +0.80 V to +1.14 V as shown in **Table 1**. Compounds with $[PF_6]^-$ and $[Cl]^-$ (**C4**–**C7**) exhibited higher $E_{1/2}$ values (+1.12 V to +1.14 V) as compared to those with $[BPh_4]^-$ anion (**C1**–**C3**, +0.80 V to

Research Article
doi.org/10.1002/ejic.202500063

Table 1. Electrochemical data for the pyrazole-pyridine Ru(II) complexes.

Compound	E_{pa}	E_{pc}	$E_{1/2}$	ΔEPe
C1[a)]	0.89	0.74	0.81	0.15
C2	0.87	0.72	0.80	0.12
C3	0.88	0.76	0.82	0.15
C4	1.18	1.09	1.14	0.09
C5	1.18	1.08	1.13	0.10
C6	1.17	1.09	1.13	0.08
C7	1.22	1.02	1.12	0.20

[a)]Conditions: 0.5 mM catalyst concentration in 0.1 M ^{t}BuNPF$_6$/MeCN, scan rate: 100 mv s^{-1}.

+0.82 V) (Figure S63, Supporting Information). This indicates that the Ru(II) center in **C4**–**C7** is more resistant to oxidation, reflecting a stronger stabilization of the Ru(II) oxidation state. Complexes **C4**–**C7** have a larger redox potential because $[PF_6]^-$ and $[Cl]^-$ are electron withdrawing and, in these examples, non-coordinating, resulting in a more electrophilic metal centre. In contrast, the lower $E_{1/2}$ values for **C1**–**C3** indicate that the Ru(III) oxidation state is less effectively stabilized and more electron rich, due to the bulkier, less electron-withdrawing character of $[BPh_4]^-$, consistent with literature precedent.[27]

2.3. Formic Acid Dehydrogenation

FADH was investigated using complexes **C1**–**C7**, as catalyst precursors under optimized conditions: 0.1 mol% pre-catalyst, 3 mmol HCOOK and 5 mmol FA in 2 mL DMSO at 100 °C (Details in Section S5, Supporting Information). The first step in determining the optimal hydrogen generation conditions was to systematically vary reaction parameters, including formates, temperature, catalyst loading, and substrate concentration. Having established optimum performance, the catalytic activity of the remaining complexes in the series was evaluated. This allowed for a comparative analysis, providing insights into the influence of ligand architecture on catalytic efficiency and identifying the most active complex within the series. All the optimized conditions were performed using **C1**. H_2 gas formation was confirmed through a combination of ^{1}H NMR and GC-TCD analysis. NMR monitoring experiments conducted in DMSO-d_6 showed a singlet at δ 4.60 ppm (Figure S2, Supporting Information), ascribed to the presence of hydrogen gas in DMSO-d_6.[28] Additionally, GC-TCD analysis using helium as the carrier gas verified the production of CO_2 with minimal CO formation (Figure S3, Supporting Information).

2.3.1. Influence of Formates

Different alkali metal formate additives containing Na, K, and Li were evaluated to find the most active one. No catalytic activity was observed in the absence of the additives. A comparative plot of TONs as a function of time revealed that the metal formates could be ranked in decreasing order of efficiency from HCOOK > HCOONa > HCOOLi (Figure S4, Supporting Information). Considering the HSAB principle, this result suggests that in our system the softer nature of potassium ions may better stabilize key intermediates or interact more favorably with the catalyst, leading to enhanced activity. Our observation of additive influence (K > Na > Li) is consistent with our previous findings[29] while contrasting with previous observations in which Lewis acid activation of FA coincides with an alkali metal order: Li > Na > K.[30] Increasing the additive concentration from 1 to 3 mmol decreased the reaction time, with full gas consumption generated in 170 and 120 min, respectively (Figure S5, Supporting Information). Further increasing the additive to 5 mmol did not improve the reaction time, suggesting that the catalytic system had reached saturation, where additional additive no longer enhances the reaction rate.

2.3.2. Influence of Solvents

Next, different organic solvents were screened in FADH with **C1**. The solvents include dimethyl sulfoxide (DMSO), dimethylformamide (DMF), triglyme, toluene, and water. From the plot of TONs with time in Figure S6, Supporting Information DMSO gave the best catalytic activity among all the solvents used, reaching TON of 560 within 140 min. Despite reaching TON of 370 in 230 min, DMF did not reach maximum conversion, plateauing after 230 min. This superior performance can be attributed to the solvent's stronger coordination ability and its stabilizing effect on key catalytic intermediates formed during FADH.[31,32] Triglyme and toluene gave TON of 119 and 61 within 180 and 60 min, respectively, while water and neat FA (TON of 63 within 110 min) demonstrate poor performance despite **C1**'s solubility in these solvents. Increasing the solvent volume from 1 to 2 mL led to slightly improved activity, likely due to better catalyst dispersion and substrate interaction. However, increasing the solvent to 3 mL resulted in decreased activity, likely due to substrate dilution reducing catalyst–substrate interactions (Figure S7, Supporting Information).

2.3.3. Effect of Catalyst Loading on Reaction Rate

Next, the catalyst loading was systematically varied in the range of 0.05–0.15 mol%, and the corresponding catalytic activity assessed. The results, summarized in Figure S8a, Supporting Information, demonstrate that an increase in catalyst loading leads to a proportional increase in catalytic activity. No evidence of saturation was observed within the tested range of catalyst concentrations. Plotting the initial rates against the catalyst concentrations (Figure S8c, Supporting Information) reveals a linear dependence, consistent with mononuclear active species in the rate-determining step.[33,34]

2.3.4. Effect of FA Concentration on Reaction Rate

Increasing the FA concentration resulted in longer reaction times, likely due to dilution effects (Figure S9a, Supporting Information). The impact of FA concentration on the reaction rate was further analyzed in Figure S9b, Supporting Information. The plot of ln[k

Research Article
doi.org/10.1002/ejic.202500063

versus ln[FA] indicates that the reaction is approximately half-order in [FA], attributable to a pre-equilibrium between FA/formate during pre-catalyst activation, while providing support that FA-mediated hydrogen production does not occur.[35,36]

2.3.5. Influence of Temperature

Variable temperature studies in the range 80–110 °C were conducted to establish key thermodynamic parameters (**Figure 3**a). At 100 °C, gas consumption occurred within 80 min, while lower temperatures (90 and 80 °C) led to longer reaction times of 120 and 250 min, respectively.[5] An Arrhenius plot revealed an activation energy (E_a) of 126 kJ mol^{-1} (Figure 3b). The activation energy extracted for the current catalyst system is double that obtained for our recently reported Ru(II) catalyst bearing pyridyl-formamidine ancillary ligands (E_a 61 kJ mol^{-1}), in a temperature range 60–100 °C.[29] This difference highlights the additional energy requirement that needs to be overcome in the current system, in comparison to reports for [{$RuCl_2$(*p*-cymene)}$_2$] (E_a = 69.1 kj mol^{-1}) and a related half-sandwich cationic complex [(η^6-C_6H_6)Ru(κ^2-NpyNHMe-8-AmQ)Cl]Cl (E_a = 87.9 kj mol^{-1}).[14,37] Similarly, an Eyring analysis extracted enthalpy and entropy of activation ($\Delta H^{\ddagger}$ and $\Delta S^{\ddagger}$) of 122 kJ mol^{-1} and −70 J K^{-1} mol^{-1}, respectively. The entropy value points to a transition state with associative character, while the activation parameters established experimentally are comparable to noble metal-mediated FADH.[29,38,39]

2.3.6. Screening of All Complexes Under Optimised Conditions

Having established the optimized conditions for FADH with **C1**, these conditions were then used to systematically screen **C2-C7**. All catalysts are active for FADH, with **C3** and **C6** showing the least activity compared to the other catalysts (**Table 2**, entries 3 and 6). Both complexes reached a plateau after ≈78 min with tons of 717 and 742, respectively (maximum theoretical TON = 1063). The low performance of **C3** is attributed to a combination of ligand steric influence, a relatively electron-rich metal, and the likely formation of quadrupole ion pairs, which hinder FA/formate approach.[15] In the case of **C6**, the expected activity would be higher since (i) complexes bearing [PF_6]$^-$ tend to form contact ion pairs (CIPs) that exert minimal steric influence and (ii) the metal is quite electrophilic. The low activity for **C6** must be a purely steric effect, influenced by the phenyl groups on ligand **L3**. The remaining complexes showed good activity (>95% gas consumption). **C2** (Table 2, entry 2) generally took a little bit longer to generate near-quantitative TON of 1004, as compared to **C1** and **C4–C7** which generated tons of 1032, 1028, 1020, and 1008, respectively (Table 2, entries 1, 4, 5, and 7). In the case of **C4** and **C5**, this correlates well with higher electrophilicity established with CV. For **C1**, **C2**, and **C7** the situation is more complex, demonstrating the fine balance between steric and electronic properties and the extent of ion pairing. With TON and TOF of 1032 and 1238 h^{-1} within 60 min, **C4** was found to be the best-performing catalyst.

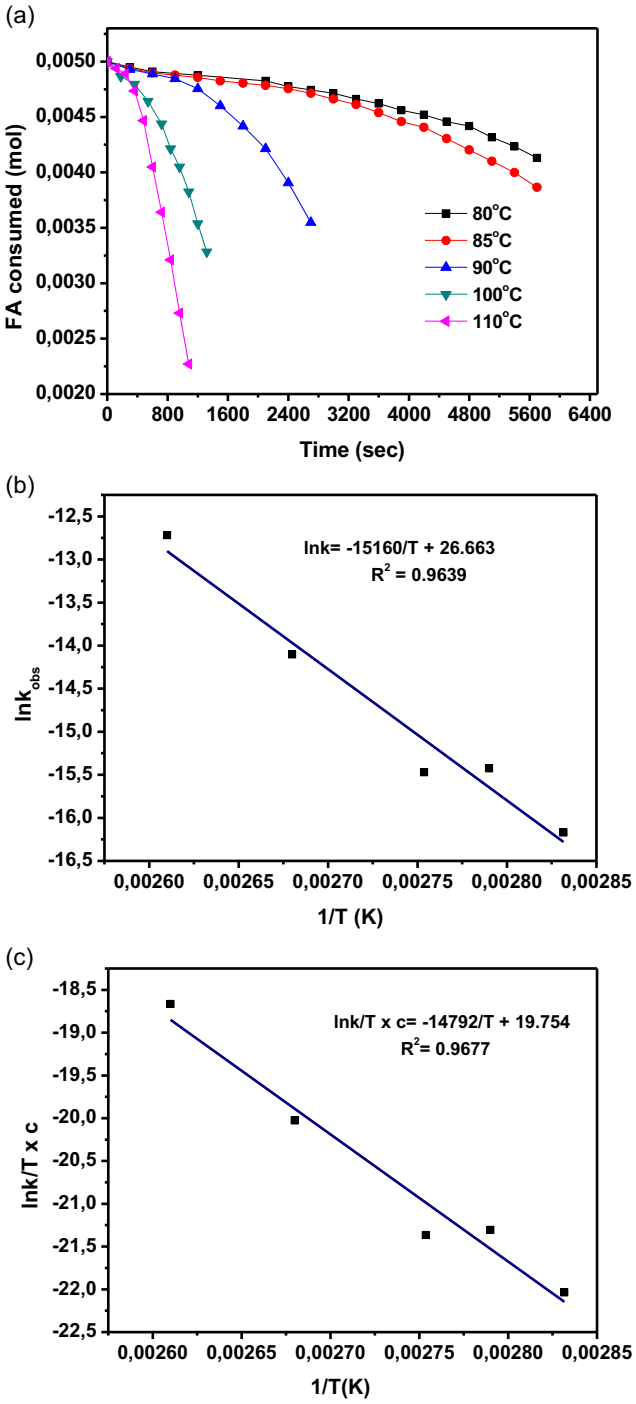

Figure 3. a) Initial FA consumption at different reaction temperatures for **C1**. Conditions: FA (5 mmol, 0.2 mL), **C1** (0.1 mol%), HCOOK (3 mmol), DMSO (2 mL). 80 °C: Rate = 1.0 × 10^{-7} mol s^{-1} (R^2 = 0.98); 85 °C: rate = 2.0 × 10^{-7} mol s^{-1} (R^2 = 0.93); 90 °C: rate = 1.91 × 10^{-7} mol s^{-1} (R^2 = 0.97); 100 °C: rate = 7.0 × 10^{-7} mol s^{-1} (R^2 = 0.97), 110 °C: rate = 3.0 × 10^{-6} mol s^{-1} (R^2 = 0.95). b) Arrhenius plot and c) Eyring plot for formic acid dehydrogenation catalyzed by **C1**.

2.3.7. Catalyst Recyclability and Stability

To evaluate the recyclability and stability of the most active pre-catalyst **C4**, repeated manual additions of FA were performed at 40-min intervals for up to six cycles. Upon the initial addition of

Table 2. Screening of complexes C1-C7 in FADH.

Entry	Compound	Time [min]	TON	TOF (max) [h^{-1}]	Conversion [%]
1[a)]	**C1**	84	1020	1129	97
2	**C2**	82	1004	1003	95
3	**C3**	80	717	903	68
4	**C4**	60	1032	1238	98
5	**C5**	74	1028	1096	97
6	**C6**	78	742	920	70
7	**C7**	76	1008	1087	96

[a)]**Conditions:** The results are the average of two readings each, with an error margin <5%. The TONs and TOFs were calculated based on the total volume of gas produced for each compound at the respective time. Catalyst: 0.1 mol%. FA: 5 mmol. HCOOK: 3 mmol. Temperature: 100 °C. Solvent: DMSO (2 mL).

FA, the catalyst exhibited a significant increase in TON, reaching ≈920, as shown in Figure S11a, Supporting Information. This steep rise reflects the high initial activity of **C4** under the optimized conditions. With subsequent additions of FA, the TON continued to increase cumulatively, reaching 1676 after the second cycle. However, a noticeable decrease in the TON increment was observed compared to the first cycle, suggesting a gradual decline in catalytic efficiency with successive FA additions. Beyond the third FA addition, the catalytic performance had reduced substantially, as evidenced by slower gas generation rates (Figure S11b, Supporting Information). By the sixth cycle, the cumulative TON plateaued at ≈3060 after 4 h of reaction time. This behavior indicates a progressive loss of catalytic activity over repeated cycles, attributable to pH-induced decomposition.[35] Continuous FA addition was employed at a controlled rate, ensuring consistent substrate concentration throughout the reaction (Figure S12, Supporting Information). Despite maintaining controlled substrate availability, the catalytic activity was notably hindered by prolonged reaction times and elevated temperatures (100 °C), leading to a gradual decline in efficiency. Over the course of the 9-h reaction, a total TON of 3170 was achieved, with a corresponding TOF of 331 h^{-1}. However, the observed decrease in activity with extended reaction times highlights the catalyst's limited stability under these operating conditions. To further investigate the stability of **C4,** we conducted an NMR study under static catalytic conditions in DMSO-d_6 (Section S6, Figure S13, Supporting Information). The J-Young NMR tube was vented periodically to mimic gas evolution and volume displacement in the experimental set-up. Within 1 h, characteristic signals corresponding to coordinated *p*-cymene disappeared, indicating its rapid dissociation. This coincided with the appearance of resonances assigned to uncoordinated **L1** and *p*-cymene. Upon further heating for 4 h, no additional spectral changes were observed. These findings suggest that under catalytic conditions, particularly during continuous or stepwise FA addition, **C4** undergoes accelerated degradation. These results underline the need for further catalyst design strategies aimed at enhanced thermal and low pH stability over extended periods.

2.3.8. Effect of Different Grades of FA

The influence of FA grade on catalytic performance was investigated by comparing 90% and 95% FA solutions under identical reaction conditions (**Figure 4**). Interestingly, the 90% FA exhibited slightly better activity than the 95% FA. These results highlight the robustness of the catalytic system, demonstrating its tolerance toward lower-grade FA, which is advantageous for practical applications where cost-effective and readily available reagents are preferred. This tolerance toward varying reagent purity levels enhances the potential for real-world applications of this catalytic system.

2.3.9. Mechanistic Considerations

To complement our kinetic and thermodynamic studies, we also conducted a kinetic isotope effect (KIE) study as shown in **Table 3**. Triethylamine (NEt_3) was used as an additive to prevent deuterium scrambling during the reaction, while HCOOD could not be evaluated due to unavailability. Substituting HCOOH with DCOOH showed only a slight reduction in reaction rate, yielding a KIE of 1.57 (Table 3, entry 2). However, when DCOOD was used as the substrate, a significantly larger decrease in reaction rate was observed, with a KIE of 3.28 (Table 3, entry 3). The findings,

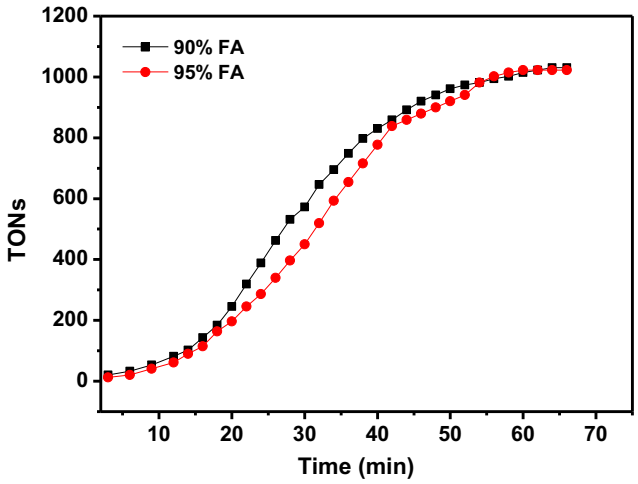

Figure 4. Influence of different FA grades on FA dehydrogenation. Conditions: Catalyst (**C4**, 0.1 mol%), DMSO (2 mL), HCOOK (3 mmol), FA (5 mmol), temperature (100 °C).

Table 3. Catalytic activity of C4 in the dehydrogenation of various FA isotopes.

Entry	Substrate	TOF [h-1]	KIE
1	HCOOH[a)]	135.31	1
2	DCOOH[b)]	116.86	1.57
3	DCOOD[c)]	59.45	3.28

[a)]Conditions: **C4** (0.1 mol%), FA (mmol), NEt_3 (1 mmol) and DMSO (1 mL) at 80 °C; [b)]TOF. Measured after 20 min of activation; [c)]Kinetic isotope effect ($TOF_{HCOOH}/TOF_{isotopologue}$).

in the absence of an assessment with HCOOD, indicate that the rate-limiting step is likely to be the cleavage of the formyl C—H bond, which happens during the decarboxylation of Ru-formate intermediate, leading to the formation of Ru-hydride.[13]

To establish the nature of Ru-hydride formation, a ^{1}H NMR study was conducted between **C4** and HCOOK. No Ru-hydride signals were detected when **C4** was dissolved in DMSO-d_6 at room temperature in the absence or presence of HCOOK (1:1 ratio). Upon heating the reaction mixture in a high-pressure J-Young NMR tube to 90 °C in a water bath, ^{1}H NMR spectra collected at various time intervals (ranging from 1 min to 22 h) revealed signals in the range $\delta = -5.5$ to -16.0 ppm, indicative of Ru-hydride species (Figure S14, Supporting Information). The observation of multiple hydride signals infers the presence of competing equilibria at low formate ratios. The ratio of catalyst to formate was increased to 1:50 to mimic the catalytic conditions used for FADH, and the reaction progress was monitored over the intervals ranging from 1 min to 20 h of heating (Figure S15, Supporting Information). We observed the formation of three different hydride species, with a prominent ^{1}H NMR signal at $\delta - 11$ ppm assigned to the formation of a primary Ru-monohydride species, consistent with our and other reports.[13,29]

2.3.10. Comparative Analysis with Reported Catalysts Systems

Table 4 tabulates activity metrics of selected catalyst systems compared to those outlined in the current study. Entries 1–4 highlights the current state of the art in metal-mediated FADH. A water-soluble Ir complex, **I**, was reported to dehydrogenate FA with TON 2.4 million in the absence of additive, at a moderate temperature of 80°.[36] A phenoxy-PYE ligated Ir-catalyst, **II**, could dehydrogenate FA under industrially relevant conditions, with 1 equivalent of HCOOLi with TONs of 2 million and steady-state TOF of 80 000.[30] Milstein's PNP-ligated Ru-hydride, **III**, could mediate FADH with TONs of 1.7 million and TOF of 3100 under neat conditions (Table 4, entry 3).[40] A related (PNP) Ru-hydride complex, **IV**, with triethylamine as additive was found to dehydrogenate FA with maximum TOF of 257,000 h^{-1} and TON of 326,500 at 90 °C in DMF (Table 4, entry 4).[41] Our group recently reported that a Ru(II) complex bearing new pyridyl-formamidine ligands, **V**, was an active catalyst when activated with HCOOK for the dehydrogenation FA, with TONs and TOFs of 7892 and 225, respectively, at 100 °C in DMSO (Table 4, entry 5).[29] Complex **C4** as catalyst precursor compares favorably to several reported systems derived from Ru and other metals. A π-coordinated phenoxy-ligated Ru-dimer, **VI**, could dehydrogenate FA with TON of 173 and $TOF_{initial}$ of 202 h^{-1} in DMSO at 90 ° (Table 4, entry 6).[42] Contrary to the robustness observed for **C4** under higher water content (90% FA), **VI** was found to be inhibited by water, which is likely responsible for lower activity. The [Ru(triphos)$(MeCN)_3$]$(OTf)_2$ system, **VII**, was reported to achieve full conversion in an hour, at a catalyst loading of 12.9 μmol (FA:cat. = 100:1) at 80 °C, with N,N-dimethyloctanamine as additive, albeit with a low TON and TOF of 1000 and 100 h^{-1}, respectively after 180 min, illustrating slower activation than with **C4**, even though **VII** is more robust than **C4** at lower [**VII**] (Table 4, entry 7).[43] As a final example, a related PCP-Ni(II)-hydride, **VIII**, dehydrogenated FA in the presence of triethylamine at 80 °C, with tons of 626, with higher CO_2 content in product gas, due to propylene carbonate cleavage (Table 4, entry 8).[44] The system described in this work distinguishes itself with low additive requirements and full substrate conversion in a short timeframe at low catalyst loadings. The identification of ligand dissociation as one of the decomposition pathways during FADH catalysis with **C4** also contributes valuable insights to the design and understanding of future FADH catalyst systems.

Table 4. Comparative analysis of various FADH catalysts with C4.

Entry	Catalyst	Additive	Solvent	*T* [°C]	TON [x10^3]	TOF [x10^3, h^{-1}]	Reference
1	**I**	–	H_2O	80	2400	375	[36]
2	**II**	HCOOLi	DMSO	80	3000	80	[30]
3	**III**	–	Neat	103	1700	3.1	[40]
4	**IV**	NEt_3	DMF	90	326	257	[41]
5	**V**	HCOOK	DMSO	100	7.892	0.225	[29]
6	**VI**	NEt_3	DMSO	90	0.173	0.202	[42]
7	**VII**	$OctNMe_2$	–	80	1.00	0.100	[43]
8	**VIII**	NEt_3	Propylene carbonate	80	0.626	.209	[44]
9	**C4**	HCOOK	DMSO	100	3.169	0.336	This work

3. Conclusions

Ru(II) complexes bearing pyrazole-pyridine ligands, **C1–C7**, were successfully synthesized and comprehensively characterized, providing electronic and steric modulation due to different counterions and ligand substituents. Optimized conditions using **C1** for FADH were established. Screening of additives revealed potassium formate as the most effective promoter, significantly enhancing catalytic performance. Kinetic studies showed a first-order dependence on catalyst concentration and half-order dependence on FA, providing evidence for a mononuclear resting state and hydrogen production involving hydronium ions. Arrhenius and Eyring analysis revealed the thermodynamic activation parameters associated with FADH for **C1**. Specifically, the E_a was established as 126 kJ mol^{-1}, whereas $\Delta H^{\ddagger}$ and $\Delta S^{\ddagger}$ were found to be 122 kJ mol^{-1} and -70 J K^{-1} mol^{-1}, respectively, indicative of associative character in the rate-determining step. Continuous FA addition proved effective in maintaining consistent substrate availability, yielding a TON of 3170 and a TOF of 331 h^{-1} after 9 h. Recyclability studies revealed that the catalyst retained activity over multiple cycles, achieving a maximum TON of 3060 after six cycles. However, a gradual decline in catalytic efficiency was observed, attributed to pH changes upon fresh FA additions and thermal instability of the catalyst under prolonged high-temperature conditions, as established by NMR spectroscopy. These findings emphasize the need for further optimization of catalyst design to enhance stability and extend catalytic lifetimes under operational conditions. A Ru-monohydride

species was detected by ^{1}H NMR spectroscopy and identified as the key intermediate species in the dehydrogenation of FA, which according to our KIE experiments, is formed by formyl C—H bond cleavage from Ru-formate.

4. Experimental Section

Materials and Methods

All experimental details pertaining to ligand and complex synthesis, as well as FADH catalysis, are provided in the sections S1–S6, Supporting Information.

X-ray Crystal Structure Determination

Crystal structure data pertaining to **C4** has been deposited with Deposition Number 421 774 (C4) contain(s) the supplementary crystallographic data for this paper. These data are provided free of charge by the joint Cambridge Crystallographic Data Centre and Fachinformationszentrum Karlsruhe Access Structures service.

Acknowledgements

The School of Chemistry, University of the Witwatersrand is thanked for infrastructure and equipment support. Prof. Manuel Fernandes (Wits University) is gratefully thanked for his assistance with SCXRD analyses. Sasol South Africa is thanked for its financial support to RM. AJS acknowledges funding support of the National Research Foundation (ZA), with grant numbers: 137758, 127291 and CPRR240312208672.

Conflict of Interest

The authors declare no conflict of interest.

Keywords: dehydrogenation · formic acid · hydrogen production · pyrazolyl-pyridine · ruthenium

[1] M. Iglesias, L. A. Oro, *Eur. J. Inorg. Chem.* **2018**, *2018*, 2125.
[2] A. Midilli, I. Dincer, *Int. J. Hydrogen Energy* **2008**, *33*, 4209.
[3] J. Guo, C. K. Yin, D. L. Zhong, Y. L. Wang, T. Qi, G. H. Liu, L. T. Shen, Q. S. Zhou, Z. H. Peng, H. Yao, *Chem. Sustainable Energy Mater.* **2021**, *14*, 2655.
[4] F. Joó, *Chem. Sustainable Energy Mater.* **2008**, *1*, 805.
[5] S. Kar, M. Rauch, G. Leitus, Y. Ben-David, D. Milstein, *Nat. Catal.* **2021**, *4*, 193.
[6] H. L. Jiang, S. K. Singh, J. M. Yan, X. B. Zhang, Q. Xu, *Chem. Sustainable Energy Mater.* **2010**, *3*, 541.
[7] N. Onishi, R. Kanega, H. Kawanami, Y. Himeda, *Molecules* **2022**, *27*, 455.
[8] G. Laurenczy, P. J. Dyson, *J. Braz. Chem. Soc.* **2014**, *25*, 2157.
[9] Y. Maenaka, T. Suenobu, S. Fukuzumi, *Energy Environ. Sci.* **2012**, *5*, 7360.
[10] Z. Wang, S. M. Lu, J. Wu, C. Li, J. Xiao, *Eur. J. Inorg. Chem.* **2016**, *2016*, 490.
[11] X. Li, X. Ma, F. Shi, Y. Deng, *Chem. Sustainable Energy Mater.* **2010**, *3*, 71.
[12] S. Günnaz, N. Özdemir, S. Dayan, O. Dayan, B. Çetinkaya, *Organometallics* **2011**, *30*, 4165.
[13] C. Guan, D. Zhang, Y. Pan, M. Iguchi, M. Ajitha, J. Hu, H. Li, C. Yao, M. H. Huang, S. Min, J. Zheng, Y. Himeda, H. Kawanami, K. W. Huang, *Inorg. Chem.* **2017**, *56*, 438.
[14] S. Patra, M. K. Awasthi, R. K. Rai, H. Deka, S. M. Mobin, S. K. Singh, *Eur. J. Inorg. Chem.* **2019**, *2019*, 1046.
[15] M. C. Joseph, I. A. Kotzé, N. J. Nnaji, A. J. Swarts, S. F. Mapolie, *Organometallics* **2022**, *41*, 3546.
[16] P. Govindaswamy, Y. A. Mozharivskyj, M. R. Kollipara, *J. Organomet. Chem.* **2004**, *689*, 3265.
[17] S. O. Ojwach, I. A. Guzei, J. Darkwa, *J. Organomet. Chem.* **2009**, *694*, 1393.
[18] H. Kotzé, S. Mapolie, *Appl. Organomet. Chem.* **2017**, *31*, e3643.
[19] J. M. Gichumbi, H. B. Friedrich, B. Omondi, *Inorg. Chim. Acta* **2017**, *456*, 55.
[20] P. Singh, A. K. Singh, *Organometallics* **2010**, *29*, 6433.
[21] T. S. Ramos, D. M. Luz, R. D. Nascimento, A. K. Silva, L. M. Lião, V. M. Miranda, V. M. Deflon, M. P. de Araujo, L. T. Ueno, F. B. C. Machado, L. R. Dinelli, A. L. Bogado, *J. Organomet. Chem.* **2019**, *892*, 51.
[22] R. Ruzziconi, G. Bellachioma, G. Ciancaleoni, S. Lepri, S. Superchi, R. Zanasi, G. Monaco, *Dalton Trans.* **2014**, *43*, 1636.
[23] F. A. Cotton, P. Lei, C. A. Murillo, L. Wang, *Inorg. Chim. Acta* **2003**, *349*, 165.
[24] R. J. Lungren, M. Stradiotto, *Ligand Design in Metal Chemistry: Reactivity and Catalysis*, 1st edition (Eds: R. J. Lundgren, M. Stradiotto), Wiley-VCH, New Jersey **2016**, p 7.
[25] M. Abrahamsson, H. C. Becker, L. Hammarström, C. Bonnefous, C. Chamchoumis, R. P. Thummel, *Inorg. Chem.* **2007**, *46*, 10354.
[26] D. A. Bardwell, J. C. Jeffery, E. Schatz, E. E. M. Tilley, M. D. Ward, *J. Chem. Soc. Dalton Trans.* **1995**, *5*, 825.
[27] V. Leandri, Q. Daniel, H. Chen, L. Sun, J. M. Gardner, L. Kloo, *Inorg. Chem.* **2018**, *57*, 4556.
[28] G. R. Fulmer, A. J. M. Miller, N. H. Sherden, H. E. Gottlieb, A. Nudelman, B. M. Stoltz, J. E. Bercaw, K. I. Goldberg, *Organometallics* **2010**, *29*, 2176.
[29] J. M. Edor, M. C. Joseph, J. H. L. Jordaan, H. C. M. Vosloo, A. J. Swarts, *Appl. Organomet. Chem.* **2025**, *39*, e70016.
[30] N. Lentz, M. Albrecht, *ACS Catal.* **2022**, *12*, 12627.
[31] S. Ge, J. Liu, L. Gong, X. Mo, C. Liu, X. Yi, P. He, *Eur. J. Inorg. Chem.* **2024**, *27*, e202300509.
[32] K. Rohmann, J. Kothe, M. W. Haenel, U. Englert, M. Hölscher, W. Leitner, *Angew. Chem. Int. Ed.* **2016**, *128*, 9112.
[33] W. Yang, G. A. Filonenko, E. A. Pidko, *Chem. Commun.* **2023**, *59*, 1757.
[34] B. C. Gates, *Royal Soc. Chem.* **2024**, *15*, 16821.
[35] G. Menendez Rodriguez, F. Zaccaria, L. Tensi, C. Zuccaccia, P. Belanzoni, A. Macchioni, *Chem. - Eur. J.* **2021**, *27*, 2050.
[36] Z. Wang, S. M. Lu, J. Li, J. Wang, C. Li, *Chem.—A Euro. J.* **2015**, *21*, 12592.
[37] J. D. Scholten, M. H. G. Prechtl, J. Dupont, *ChemCatChem* **2010**, *2*, 1265.
[38] S. Fukuzumi, T. Kobayashi, T. Suenobu, *ChemSusChem* **2008**, *1*, 827.
[39] O. Manuel, I. Enrique, *Angew. Chem. Int. Ed.* **2009**, *48*, 4800.
[40] S. Kar, M. Rauch, G. Leitus, Y. Ben-David, D. Milstein, *Nat. Catal.* **2021**, *4*, 193.
[41] G. A. Filonenko, R. Van Putten, E. N. Schulpen, E. J. M. Hensen, E. A. Pidko, *ChemCatChem* **2014**, *6*, 1526.
[42] R. Verron, E. Puig, P. Sutra, A. Igau, C. Fischmeister, *ACS Catal.* **2023**, *13*, 5787.
[43] I. Mellone, M. Peruzzini, L. Rosi, D. Mellmann, H. Junge, *Dalton Trans.* **2013**, *42*, 2495.
[44] S. Enthaler, A. Brück, A. Kammer, H. Junge, E. Irran, S. Gülak, *ChemCatChem* **2015**, *7*, 65.

Manuscript received: February 7, 2025
Revised manuscript received: March 12, 2025
Version of record online: May 30, 2025